journal of the mechanical behavior of biomedical materials 152 (2024) 106414

Contents lists available at ScienceDirect

Journal of the Mechanical Behavior of Biomedical Materials

journal homepage: www.elsevier.com/locate/jmbbm

Comparison of two contrast-enhancing staining agents for use in X-ray imaging and digital volume correlation measurements across the cartilage-bone interface

Sarah Davis [a,b,*], Aikaterina Karali [b], Tim Balcaen [c,d,e], Jurgita Zekonyte [b], Maïté Pétré [c,d,f], Marta Roldo [a], Greet Kerckhofs [c,d,g,h,1], Gordon Blunn [a,1]

[a] School of Pharmacy and Biomedical Science, University of Portsmouth, Portsmouth, PO1 2DT, UK
[b] School of Mechanical and Design Engineering, University of Portsmouth, PO1 3DJ, UK
[c] Biomechanics Lab, Institute of Mechanics, Materials and Civil Engineering, UCLouvain, Louvain-la-Neuve, Belgium
[d] Pole of Morphology, Institute of Experimental and Clinical Research, UCLouvain, Brussels, Belgium
[e] Molecular Design and Synthesis, Department of Chemistry, KU Leuven, Leuven, Belgium
[f] Biomechanics Section, Department of Mechanical Engineering, KU Leuven, Heverlee, Belgium
[g] Department of Materials Engineering, KU Leuven, Heverlee, Belgium
[h] Prometheus, Division for Skeletal Tissue Engineering, KU Leuven, Leuven, Belgium

ARTICLE INFO

Keywords:
Contrast-enhanced X-ray computed tomography
Cartilage-bone interface
Digital volume correlation
Cartilage mechanics

ABSTRACT

Objective: The pathogenesis of osteoarthritis (OA) is associated with subchondral bone changes, which is linked to abnormal strain distribution in the overlying articular cartilage. This highlights the importance of understanding mechanical interaction at the cartilage-bone interface. The aim of this study is to compare solutions of two contrast-enhancing staining agents (CESA) for combining high-resolution Contrast-Enhanced X-ray microfocus Computed Tomography (CECT) with Digital Volume Correlation (DVC) for full-field strain measurements at the cartilage-bone interface.

Design: Bovine osteochondral plugs were stained with phosphotungstic acid (PTA) in 70% ethanol or 1:2 hafnium-substituted Wells-Dawson polyoxometalate (Hf-WD POM) in PBS. Mechanical properties were assessed using micromechanical probing and nanoindentation. Strain uncertainties (from CECT data) were evaluated following two consecutive unloaded scans. Residual strains were computed following unconfined compression (*ex situ)* testing.

Results: PTA and Hf-WD POM enabled the visualisation of structural features in cartilage, allowing DVC computation on the CECT data. Residual strains up to ~10,000 με were detected up to the tidemark. Nanoindentation showed that PTA-staining caused an average ~6-fold increase in articular cartilage stiffness, a ~19-fold increase in reduced modulus and ~7-fold increase in hardness, whereas Hf-WD POM-stained specimens had mechanical properties similar to pre-stain tissue. Micromechanical probing showed a 77% increase in cartilage surface stiffness after PTA-staining, in comparison to a 16% increase in stiffness after staining with Hf-WD POM.

Conclusion: Hf-WD POM is a more suitable CESA solution compared to PTA for CECT imaging combined with DVC as it allowed visualisation of structural features in the cartilage tissue whilst more closely maintaining tissue mechanical properties.

1. Introduction

Osteoarthritis (OA) is a degenerative joint disease that affects over 500 million people worldwide, which is increasing due to an ageing population (Hunter et al., 2014, 2020; Martel-Pelletier et al., 2016). The pathogenesis of OA is associated with changes in subchondral bone, such as microdamage, subchondral bone sclerosis, the formation of bone marrow lesions and increased bone remodeling (Goldring and Goldring,

* Corresponding author. School of Pharmacy and Biomedical Science, University of Portsmouth, Portsmouth, PO1 2DT, UK.
E-mail address: sarah.davis@port.ac.uk (S. Davis).
[1] Joint last authors.

https://doi.org/10.1016/j.jmbbm.2024.106414
Received 8 March 2023; Received in revised form 11 December 2023; Accepted 19 January 2024
Available online 20 January 2024

2016; Burr and Gallant, 2012; Wang et al., 2010). These structural changes are thought to be associated with abnormal strain distribution in the overlying cartilage and disrupt load transfer throughout the entire osteochondral unit (Zhen et al., 2021). This highlights the complex interrelationship between articular cartilage and subchondral bone during early-stage OA and the importance of measuring strain changes at the interface, which will allow a better understanding of the mechanical interactions involved in the pathogenesis of OA for improved treatments (Davis et al., 2021).

Strain measurements of the cartilage-bone interface have been limited to 2D surface analysis using Digital Image Correlation (DIC) (Shaktivesh and Lee, 2019; Gao et al., 2013; Sztefek et al., 2010), but since these biological tissues have a complex and heterogenous architecture it is important to assess strain changes in 3D to understand the full interplay of strain distribution throughout tissue. Techniques such as high-resolution X-ray Computed microfocus Tomography (XCT) combined with digital volume correlation (DVC), are able to assess 3D full-field strain changes, including residual strains (Peña Fernández et al., 2020) and have been used to quantify strains in bone (Gillard et al., 2014; Tavana et al.; Tavana et al., 2020), across the bone-cartilage interface (Tozzi et al., 2020) and across bone-biomaterial interfaces (Peña Fernández et al., 2019). However, DVC requires contrast difference between the different tissue constituents, which is hard to achieve in unmineralised tissues such as cartilage due to low X-ray attenuation. Phase-contrast imaging has shown to enhance grayscale features in unmineralised tissue for XCT imaging (Tozzi et al., 2020). However, this results in lengthy acquisition times in which the specimen is subject to high X-ray exposure. Alternatively, tissue staining with contrast-enhancing staining agents (CESAs), including mercury (II) chloride ($HgCl_2$), phosphomolybdic acid (PMA) (Pauwels et al., 2013), cationic or anionic iodinated CESAs (Lusic and Grinstaff, 2013; Yoo et al., 2011; Gao et al., 2021; Stewart et al., 2017) or phosphotungstic acid (PTA) (Clark et al., 2020; Nieminen et al., 2017), can be used in combination with lab-based XCT (further referred to as contrast-enhanced XCT or CECT) and allow three-dimensional (3D) imaging of articular cartilage at the cellular level. However, since certain combinations of CESAs with certain solvents might result in tissue alterations (e.g., shrinkage, dehydration), the mechanical properties of the tissue might be altered upon contrast-enhancement. For example, some routinely used CESAs, such as PTA, are often dissolved in ethanol (EtOH), which modifies the water content of the tissue and hence the mechanical properties, and is, not representative of an *in vivo* environment. Therefore, further research is needed to understand the effect of CESA solutions on the mechanical properties of osteochondral tissues prior to analyzing strain distribution using CECT imaging/DVC. Recently, Kerckhofs et al. (2018) reported on a polyoxometalate structure, i.e., 1:2 hafnium-substituted Wells-Dawson polyoxometalate (Hf-WD POM), which showed no effect on tissue morphology and allowed the visualisation of tissue microstructure of articular cartilage and other unmineralised tissues in mouse joints (Kerckhofs et al., 2018; de Bournonville et al., 2020). However, the effect of this CESA on the mechanical properties of cartilage has not yet been investigated.

The aim of this study is to compare two CESA solutions; PTA in ethanol and Hf-WD POM in PBS for their potential to generate sufficient contrast of articular cartilage features during CECT imaging, and to analyse the effect of the CESA solutions on tissue mechanical properties. Additionally, the suitability of DVC for analyzing the strain patterns from the CECT datasets for regions of cartilage and mineralised tissues (calcified cartilage and subchondral bone) will be determined, and the full-field strain uncertainties and post-mechanics residual strains of the entire cartilage-bone unit will be evaluated.

2. Materials and methods

2.1. Experimental design

Bovine osteochondral plugs underwent a testing protocol (Fig. 1) which compared the effect of the two staining solutions (PTA in ethanol and Hf-WD POM in PBS) on tissue mechanical properties. We assessed the ability of each CESA to resolve recognizable microstructural features in articular cartilage and mineralised tissue during CECT imaging for improving DVC correlation for strain analysis at the bone-cartilage interface. Micromechanical probing of the cartilage articular surface was conducted on fresh unstained specimens, after the staining procedure, and after acquiring two consecutive CECT datasets for DVC zero-strain analysis (Fig. 1A). Mechanical testing (unconfined compression) was performed to induce plastic deformation and the specimens were immediately re-imaged using CECT to compute DVC residual strains (Fig. 1A). Nanoindentation (Fig. 1B) was performed on osteochondral specimens before and after staining to analyse the effect of the CESA solution across the bone-cartilage interface.

2.2. Specimen preparation and staining

Cylindrical osteochondral plugs (Ø = 4 mm, H = 8 mm; and Ø = 10 mm, H = 8 mm) from adult bovine knee joints (n = 5) were cored from the medial condyle of the tibias (Fig. 1A), and stored wrapped in parafilm at −20 °C. Before use, tissue specimens were thawed at room temperature, and hydrated in phosphate buffered saline (PBS, 1x, pH 7.4) (P4417, Sigma-Aldrich, MA, USA) for 30 min. The 4 mm plugs (n = 6 for each CESA solution) were used for the CECT imaging/DVC test protocol (Fig. 1A), whereas 10 mm diameter specimens (n = 3 for each CESA solution) (Fig. 1B) were cut in half longitudinally for nanoindentation using a PBS irrigated annular diamond wheel (Leica SP1600 saw microtome, Leica microsystems Inc., IL, USA). Both sets of specimens were stained at room temperature using either (Hunter et al., 2020) 1% w/v PTA (79690, Sigma-Aldrich, MA, USA) in 70% v/v ethanol (EtOH) (pH 2.3) for 21 h following 30 min dehydration steps in increasing concentrations of EtOH (Clark et al., 2020) or (Martel-Pelletier et al., 2016) 3.5% w/v Hf-WD POM (pH 7.0; synthesized at KU Leuven/UCLouvain) (Kerckhofs et al., 2018; Kato et al., 2006) in 1x PBS for 72 h.

2.3. Micromechanical probing, mechanical testing and nanoindentation

For micromechanical probing, osteochondral specimens were mounted on metal endcaps with epoxy (Devcon Ltd, Kent, UK) and were submerged in PBS throughout the test. Micromechanical probing was performed using a FT-RS1002 Microrobotic System with a FT-S10000 Microforce sensing probe (FemtoTools, Buchs Switzerland) by indenting in triplicate in a grid (spacing 100 μm) across the central cartilage surface using a previous method (Tozzi et al., 2020). The contact stiffness S = dP/dh, where P = indentation load (N) and h = indentation depth (μm), was calculated from the linear slope of the unloading curve after reaching the maximum load P_{max} (Oliver and Pharr, 2004). Hardness was calculated from the load over the contact area of the indentation (Oliver and Pharr, 2004).

Unconfined displacement-control compression testing (Bose Electroforce 3000, New Castle, DE, USA) involved applying a preload of 0.2 N for 3000 s to the articular cartilage surface and then applying one cycle of compressive load as a displacement of 10% of the cartilage thickness and a load frequency of 1 Hz (Santos et al., 2019) using WinTest 7 software (Bose, New Castle, DE USA). The maximum load corresponded to 3% strain and was held for 30 min to allow for stress relaxation. Following unconfined compression, the load was removed and the sample was immersed in PBS for 30 min prior to XCT imaging.

Quasi-static nanoindentation (Hysitron TI Premier Nanoindenter, Bruker, US) using a standard diamond Berkovich tip (TI-0039, Bruker,

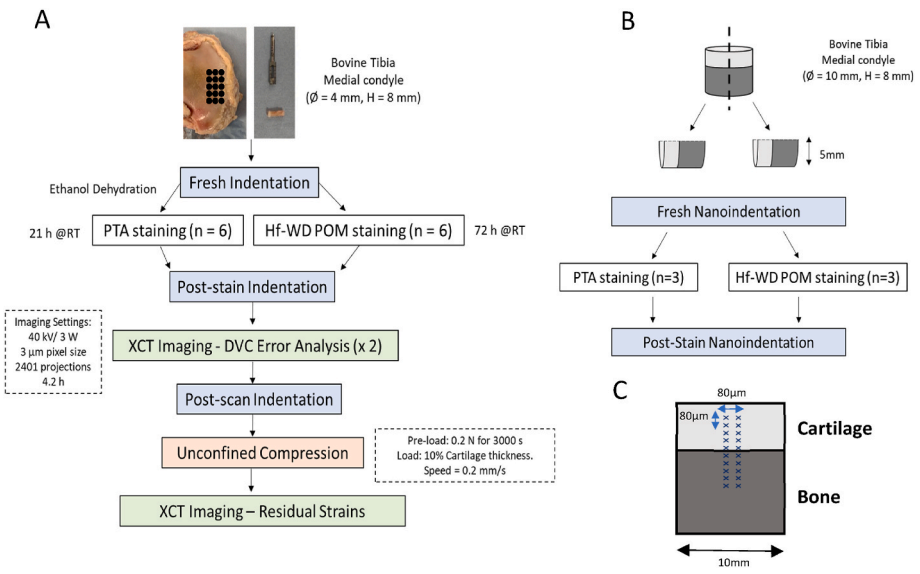

Fig. 1. Schematic representation of the experimental protocols for both PTA- and Hf-WD POM-stained specimens undergoing (A) micromechanical probing, CECT imaging, and compressive loading for residual strain distribution analysis and (B) nanoindentation across the bone-cartilage interface prior to and after staining. Drilled areas are illustrated by black circles. (C) Indentations were performed in duplicate across the central region if the osteochondral specimen, spaced 80 µm apart and spanning above and below the cartilage-bone interface.

US) was performed in duplicate at the central region of the osteochondral specimen, with a grid of 10 × 2 indentations, spaced 80 µm apart, spanning above and below the cartilage-bone interface. Specimens were hydrated while testing and a load of 10 µN was applied using TriboScan software (TriboScan Professional, Hysitron, Bruker, US). Data output included force-displacement curves, stiffness (S), hardness (H), and reduced indentation modulus (E_r) and was normalized as a percentage from the corresponding fresh, pre-stain levels for each specimen.

2.4. X-ray Computed Tomography, image post-processing and synthetic deformation

Specimens were mounted in sealed polyamide tubes and imaged in corresponding solution (PBS or 70% EtOH using a high-resolution 3D X-ray microscope (Versa 520, Zeiss, Germany). Imaging was performed at 40 kV/3 W, with a voxel size of 3 µm, 4 s exposure time and 2401 projections. Two consecutive sets of images with no load applied were obtained for DVC zero-strain analysis. Specimens were re-imaged immediately after compression to analyse residual strains. The reconstructed datasets were resliced using Fiji software (Schindelin et al., 2012) (v1.8, ImageJ, USA), rigidly aligned using the first dataset as a reference (Avizo v9.4, ThermoFisher, Waltham, MA, USA) and cropped to contain cubic volumes of interest (VOIs) from the centre of the specimen. Images were denoised by applying a Non-Local Means (NLM) filter and the regions of bone and cartilage were individually labelled using the watershed segmentation algorithm and binarized separately for each tissue type (Avizo v9.4, ThermoFisher, Waltham, MA, USA). The bottom of the deformed image of the subchondral bone was aligned to the image prior to loading using rigid registration (Avizo, v9.4, ThermoFisher, Waltham, MA, USA).

2.5. Digital volume correlation

DVC (DaVis, v10.05, LaVision Ltd., Goettingen, Germany) computation was performed to assess error uncertainties in terms of mean absolute error (MAER) and standard deviation of the error (SDER) from two consecutive zero-strain images MAER and SDER were computed for the entire VOI, and separately for the articular cartilage and mineralised tissue at the interface after cropping and masking each tissue separately. Subvolumes for DVC error analysis ranged from 50 to 150 voxels. DVC using LaVision software is based on a local approach of direct correlation between reference and deformed datasets. Residual strain distribution in the osteochondral unit following *ex-situ* compression was computed using multi-pass DVC (using predictor subvolumes 150–130 - 110–90 voxels) with a final subvolume size of 90 voxels. The third principal strain (ε_{p3}) and shear strain (γ) were computed between the first and the deformed datasets. DVC computed 3D strain maps were overlaid onto the CECT dataset (Avizo v9.4, ThermoFisher, Waltham, MA, USA).

2.6. 2D histology

Specimens (4 mm) were fixed in 10% v/v neutral-buffered formalin (NBF) (pH 6.90–7.10) (HT501128; Sigma-Aldrich, MA, USA) for 24 h and decalcified in 10% w/v ethylenediaminetetraacetic acid (EDTA) (ED-1Kg, #BCCB3404, Sigma-Aldrich, MA, USA) (pH 7.4) for 1–2 weeks prior to paraffin wax embedding. Sections of 5 µm were mounted on Superfrost plus slides (Thermofisher, Waltham, MA, USA) and histologically stained using Hematoxylin and Eosin Y (H&E) (MH51; HT110116; Sigma-Aldrich, MA, USA) using a routine histological protocol (Schmitz et al., 2010). Sections were mounted with DPX (#06522; Sigma-Aldrich, MA, USA) and imaged using a DMi1 light microscope with MC170 camera (Leica microsystems Inc., IL, USA).

2.7. Statistical analysis

All data and statistical analysis were performed using GraphPad Prism 8.02 (GraphPad Software, San Diego, California USA). Data are represented as mean (±95% Confidence Interval (CI)) where a p-value of <0.05 was considered statistically significant. Gaussian distribution was assessed using a Shapiro-Wilk normality tests where $\alpha = 0.05$. All data was normally distributed. The surface micromechanical probing data (stiffness) and nanoindentation data (stiffness, hardness, and reduced modulus) were averaged from multiple indents and analysed using either two-way analysis of variance (ANOVA) tests with Sidak's multiple comparisons tests to compare the significance of time points: fresh, stained and post-scan) or by using unpaired t-tests to assess the % change in mechanical properties between the two staining groups (PTA and Hf-WD POM) compared to corresponding fresh pre-stain levels. Since sphericity was not assumed, the Geisser-Greenhouse correction was used for the micromechanical probing data. The statistical

significance of DVC errors (MAER and SDER) for the whole imaging dataset and the cartilage and bone regions separately, were calculated using multiple t-tests for each sub-volume and were corrected for multiple comparisons using Holm-Sidak method with a statistical significance level of $\alpha = 0.05$.

3. Results

3.1. Contrast-enhanced XCT imaging

Staining with the PTA and Hf-WD POM solutions showed enhanced greyscale contrast within the articular cartilage, increasing the ability to image and resolve different microstructural features such as the organization of chondrocytes and their surrounding lacunae in the articular cartilage, as confirmed by histology. The CECT datasets also allowed detailed visualisation of the subchondral bone and its microstructure (Fig. 2). These microstructural features are critical for DVC computation.

3.2. Tissue mechanical testing

3.2.1. Micromechanical probing

Staining osteochondral specimens with the PTA/ethanol solution resulted in a significant increase in articular cartilage surface stiffness 77% (from 0.62 to 1.10 mN/μm, $p < 0.0001$; 95% CI [−0.591, −0.370]) (Fig. 3). In comparison, there were no significant differences observed with the use of the Hf-WD POM/PBS solution (from 0.71 to 0.82 mN/μm; $p = 0.182$; 95% CI [−0.275, 0.054]). The cartilage stiffness of Hf-WD POM-stained specimens was also maintained at a similar level (0.81 mN/μm; $p = 0.999$; 95% CI [−0.070, 0.076]) following a combined total of 8 h of CECT imaging (Fig. 3A), whereas PTA-stained specimens showed that surface stiffness had reduced to 0.77 mN/μm post-scan ($p = 0.0036$; 95% CI [0.153, 0.504]) (Fig. 3).

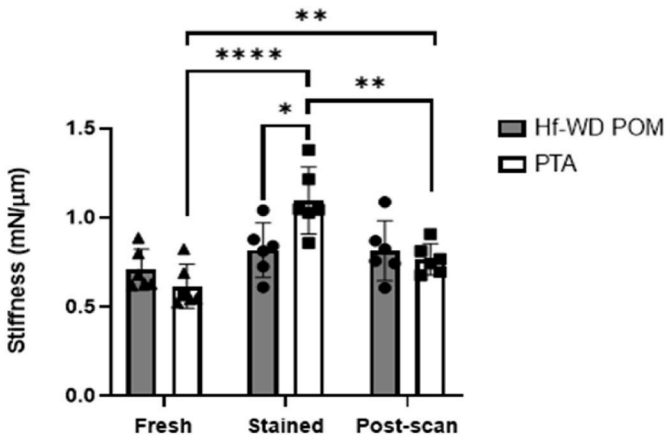

Fig. 3. Mechanical properties of specimens stained with the PTA/ethanol, Hf-WD POM/PBS solution or unstained controls showing (A) the mean stiffness (±95% CI) of articular cartilage following micromechanical surface probing (n = 6) using a paired repeated measures Two-way ANOVA with Geisser-Greenhouse correction and Sidak's Multiple Comparison Test (*p = 0.045, **p < 0.01, ****p < 0.0001). C) Nanoindentation.

The nanoindentation results showed a ~6-fold (±1.6) increase in articular cartilage (AC) stiffness after staining with a PTA/ethanol

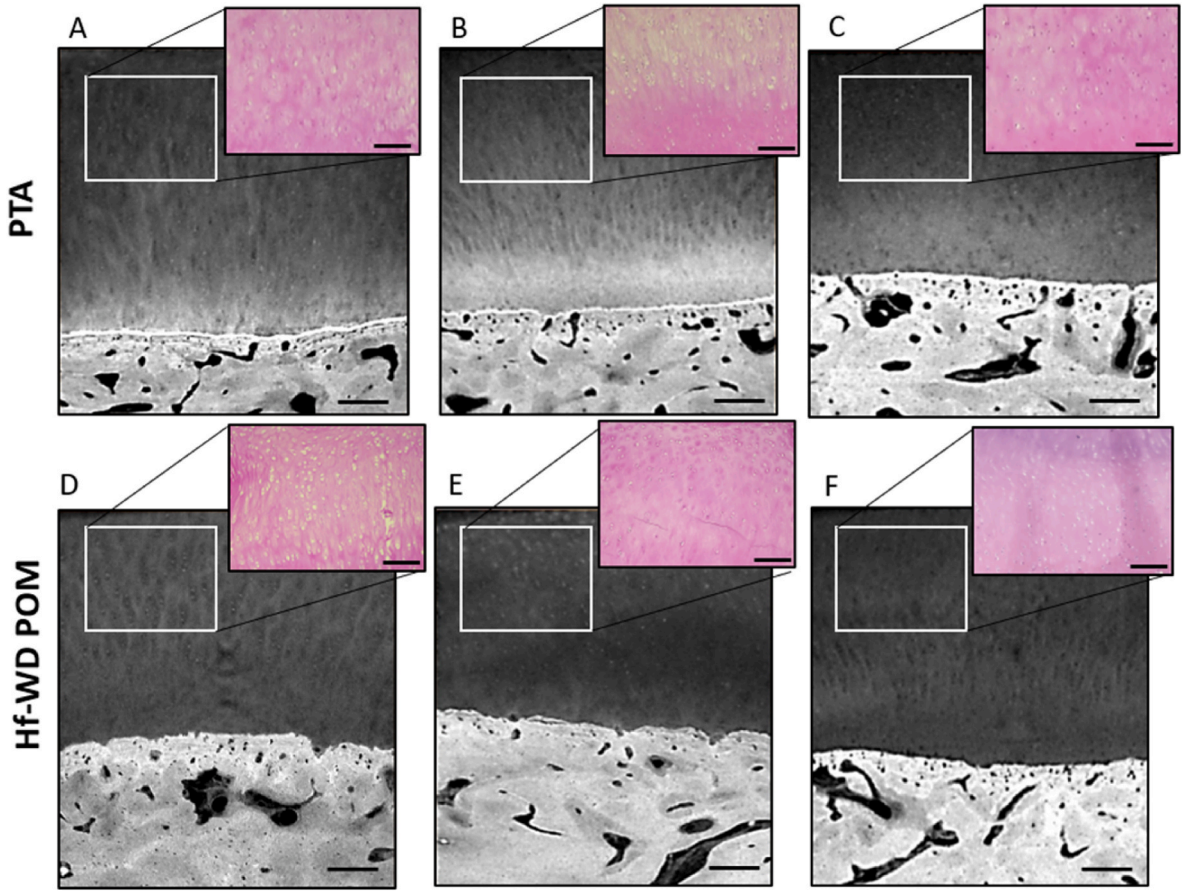

Fig. 2. Cross-sectional CECT images of osteochondral specimens, comprising of articular cartilage (dark grey region), the mineralised cartilage (including chondrocyte lacunae) and the subchondral bone regions, stained with PTA (A–C) or Hf-WD POM (D–F) (Scale bars = 300 μm or with details of corresponding histological H&E sections from the same specimens (Scale bars = 150 μm).

solution, which was significantly higher than the ~0.6-fold (±0.43) increase in AC stiffness after staining with Hf-WD POM/PBS (**p = 0.005; Fig. 4A). Subchondral bone (SB) stiffness was comparable between staining groups with a % change of 40.8 (±21.8) increase after staining with the Hf-WD POM/PBS solution and a % change of 41.9 (±32.6) in stiffness after staining with PTA/ethanol (p = 0.961; Fig. 4A). In addition, a ~19-fold (±4.4) increase in the reduced indentation modulus (E_r) (Fig. 4B), and a ~7-fold (±2.5) increase in hardness (H) (Fig. 4C) was also observed after staining fresh specimens with PTA/ethanol. This was significantly higher compared to the average 0.7-fold (±0.47), and 1.3-fold (±0.77) increase in E_r (Fig. 4B; **p = 0.002) and H (Fig. 4C; *p = 0.025) that was observed after staining with Hf-WD POM/PBS. The E_r and H of SB were not significantly different between staining groups (E_r: p = 0.64, Fig. 4B; H: p = 0.82, Fig. 4C) with an average % change of 16.89 (±32.9) and 32.35 (±41.1) in the reduced modulus (Fig. 4B); and an average % change of 13.72 (±34.3) and 20.36 (±34.3) in hardness (Fig. 4C) after staining with Hf-WD POM and PTA respectively.

3.3. DVC error uncertainties

DVC error uncertainty analysis showed that the average MAER and SDER from all samples (n = 3) follow a typical trend of decreasing DVC errors with increasing sub-volume size (ranging from 50 to 150 voxels) for both Hf-WD POM- (Fig. 5A–C) and PTA-stained (Fig. 5D–F) specimens. Throughout the error analysis, the values for SDER were consistently lower than the MAER. No significant differences were observed between average MAER for specimens stained with either Hf-WD POM/PBS solution (ranging from 1429 με [95% CI = 1920, 938] at 50 voxels to 216 με [95% CI = 395, 36] at 150 voxels) (Fig. 5A–E, I) or PTA/ethanol solution (ranging from 1381 με [95% CI = 1501, 1262] at 50 voxels to 346 με [95% CI = 423, 270] at a sub-volume of 150 voxels) (Fig. 5 B, F, J). The variability between specimens was higher for Hf-WD POM-stained specimens, particularly for the average SDER (Fig. 5D), which ranged from 1509 με [95% CI = 2196, 821] to 306 με [95% CI = 655, −43]. In contrast, the SDER of PTA-stained specimens, ranged from 858 με [95% CI = 1292, 423] to 126 με [95% CI = 220, 31].

To determine the areas of highest uncertainty, the images were segmented, and the articular cartilage (Fig. 5E and F) and mineralised cartilage/subchondral bone regions (Fig. 5 I, J) were individually cropped and masked from the CECT dataset. The areas of highest DVC error were observed in the articular cartilage with MAER values ranging from 2032 με [95% CI = 3366, 699] to 477 με [95% CI = 876, 78] in Hf-WD POM-stained specimens and from 1713 με [95% CI = 2066, 1359] to 581 με [95% CI = 1274, −112] in the PTA-stained group (Fig. 5G), whereas the precision of DVC errors (SDER) ranged from 954 με [95% CI = 1464, 444] to 151 με [95% CI = 366, 64] and from 640 με [95% CI = 748, 533] to 83 με [95% CI = 233, −67] for Hf-WD POM-stained and PTA-stained specimens respectively (Fig. 5H). In contrast, in the subchondral bone region only, the both the average MAER (<458 με Hf-WD POM [95% CI = 557,359]; <799 με PTA [95% CI = 1118, 479]) and average SDER (<220 με Hf-WD POM [95% CI = 322, 118]; <397 με PTA [95% CI = 553, 241]) values were consistently lower at all sub-volume sizes (50–150 voxels). Although in the articular cartilage region, inter-specimen variability was higher in the Hf-WD POM-stained group, in the subchondral bone region only, the variability was higher in PTA-stained specimens, particularly at smaller sub-volume sizes (~50–110 voxels). Overall, no significant differences in DVC error uncertainties were observed between the two CESA solutions, suggesting the suitability of both stains for DVC.

3.4. Residual strains

Third principal (compressive) strains (ε_{p3}) of up to ~ 10,000 με were detected in regions in the deep zones of hyaline cartilage up to the tidemark above the cartilage-bone interface in both the PTA-stained (Fig. 6 C, D) and Hf-WD POM-stained (Fig. 6 G, H) specimens, which decreased throughout the mineralised cartilage and subchondral bone. Areas of lowest strains (~0–1500 με) were apparent in superficial and middle zones of the articular cartilage region in PTA-stained specimens, in comparison to Hf-WD POM-stained specimens, which had higher but more distributed ε_{p3} strains (~2000–4000 με) throughout these cartilage zones (Fig. 6 F, G). PTA-stained specimens had greater ε_{P3} strain in the zones of mineralised cartilage and subchondral bone region than Hf-WD POM-stained specimens, in which the subchondral bone was the area of lowest strain (Fig. 6 D, H). Additionally, PTA-stained specimens had a higher spread of maximum strain distribution (up to ~10,000 με) of shear strain (γ) throughout the volume of articular cartilage (Fig. 7 C, G), whereas in Hf-WD POM-stained specimens the strain was localised in the deep zone of articular and mineralised cartilage.

4. Discussion

This study showed that both Hf-WD POM and PTA improve contrast of cartilage tissue microstructure for CECT imaging of dissected tissue plugs. This allowed microstructural feature recognition in both the articular cartilage and mineralised tissue regions and allowed subsequent DVC computation and analysis of residual strain distribution across the osteochondral interface.

DVC uncertainty tests (such as zero strain tests) must be performed to evaluate the reliability of the strain measurements after *in situ* or *ex-situ* loading. The accuracy and precision of DVC can be affected by many factors, including the quality of the input image in which regions of lower intensity correlate with higher strain errors (Liu and Morgan, 2007). Although the staining intensity varies between the specimens in this study, the areas of brighter regions were consistent between the two pre-load and post-load tomograms and is therefore unlikely to have increased these error values. The results from this study are in alignment

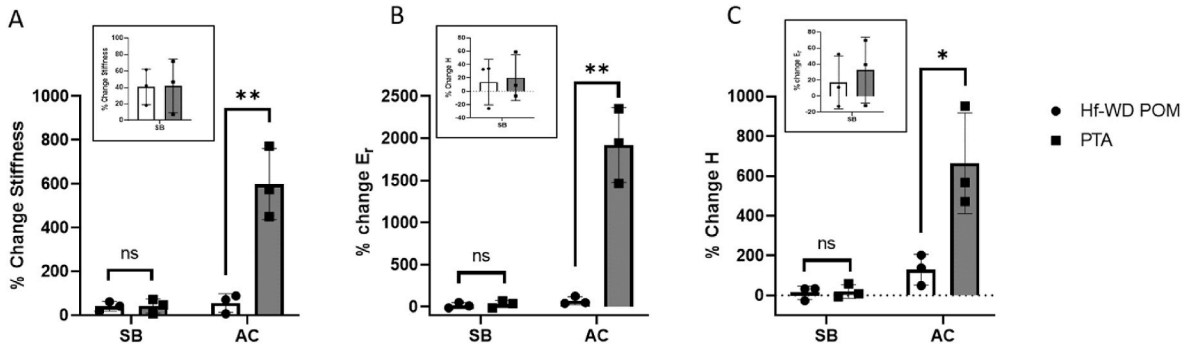

Fig. 4. Nanoindentation of subchondral bone (SB) and articular cartilage (AC) showing the average % change of stiffness (A), indentation modulus (E_r) (B) and hardness (H) (C) after staining with either Hf-WD POM/PBS solution or PTA/ethanol solution. Data represented as the mean (±95% SD) of the average of up to 20 indentations (n = 3). Significance was determined using t tests (*p = 0.025; **p < 0.01; ns = not significant).

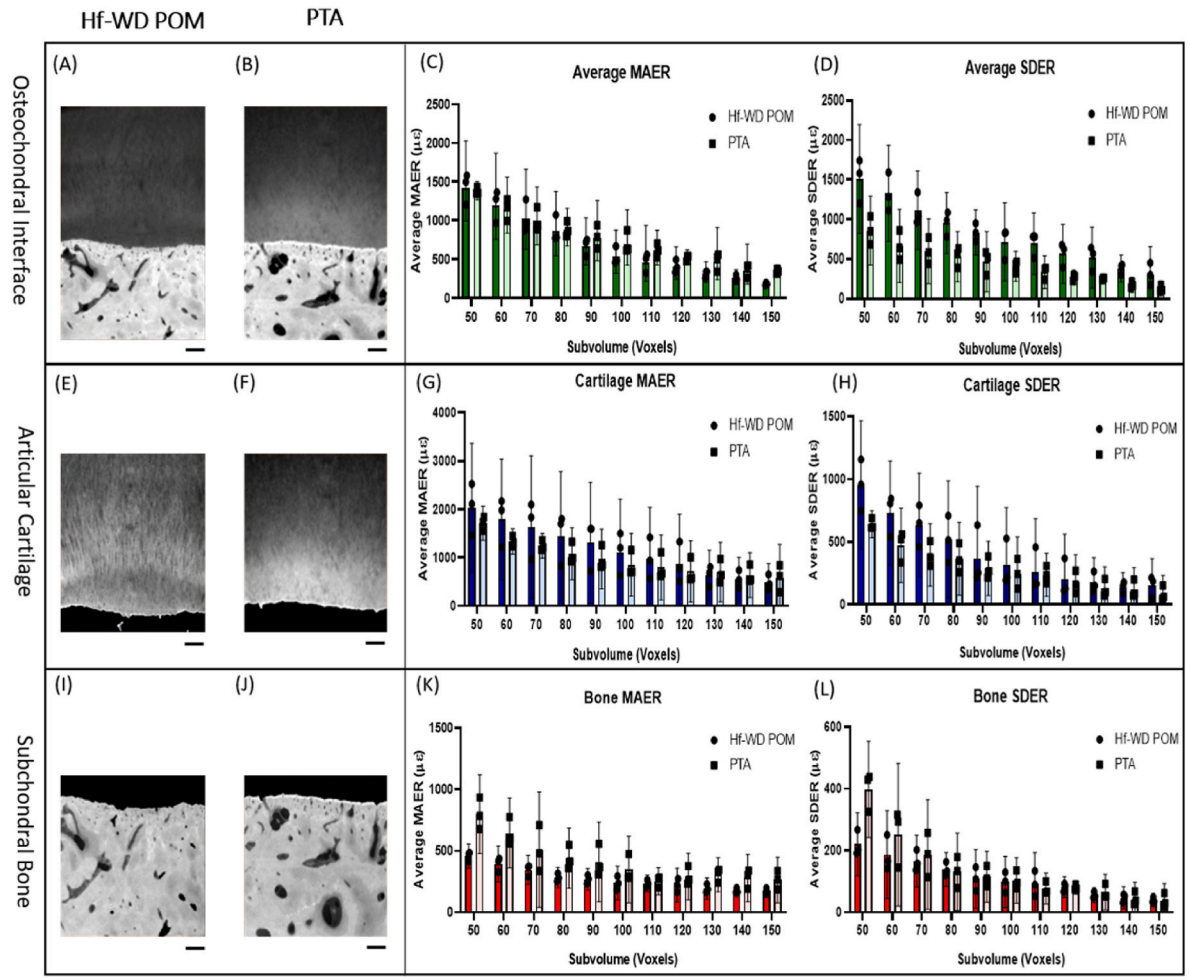

Fig. 5. DVC strain error analysis of CECT datasets. (A, B) Cross-sectional CECT images including microstructural features in the whole dataset (A, B) or in the individually cropped and masked articular cartilage (E, F) or subchondral plate/bone regions (I, J) of specimens stained with either Hf-WD POM/PBS solution (A, E, I), or PTA/ethanol solution (B, F, G). Strain uncertainty represented as average mean absolute error (MAER) (B, G, K) and average standard deviation of the error (SDER) (D, H, L) across the cartilage-bone interface for each corresponding dataset at a range of sub-volume sizes (50–150 voxels). Data are reported as mean ± 95% CI (n = 3). Scale Bars = 300 μm. Statistical significance (α = 0.05) determined using multiple t tests (without assumptions of a consistent SD) and corrected using Holm-Sidak method. Note that different scales are used.

with published data demonstrating that increasing the subvolume size results in lower DVC strain errors (Dall'Ara et al., 2017; Dall'Ara et al., 2014). It is well documented that DVC errors increase in subvolumes comprised of fewer voxels for all imaging modalities and sample types. Subvolumes for DVC error analysis ranged from 50 to 150 voxels with a voxel size of 3 μm. The average human mature chondrocyte diameter is approximately 13 μm. In this study a final subvolume of 90 voxels was used which provides a compromise between acceptable DVC error and localised measurement of cartilage deformation. The final subvolume size is often a compromise between maintaining sufficient spatial resolution yet minimizing strain errors. It is generally accepted that the maximum error criterium is below 10% of the yield strain, which would equate to DVC error uncertainties of <60,000 με for bovine articular cartilage (Madi et al., 2020; Varga et al., 2007; Burgin and Aspden, 2007). In this study, all of the DVC errors are below 1% of the yield strain. Additionally, cartilage physiologically strains at 10% which equates to 100,000 με and the residual strains observed at the interface equate to 1% (~10,000 με). Considering the mechanical approach used in this study, in which the apparent strain reached a maximum of 30,000 με, and the strain on the microscale from DVC analysis reached a maximum of 10,000 με, the DVC errors (at subvolume of 90 voxels) are below 3.5% and 10% respectively.

Overall, no significant differences in DVC error uncertainties were observed between Hf-WD POM- and PTA-stained specimens, suggesting the suitability of both CESAs for applications involving CECT and subsequent DVC (Fig. 5). Since DVC error analysis can be affected by sample variation such as composition, microstructure, anatomical location and image quality, causing differences up to three-fold in accuracy and precision (Liu and Morgan, 2007), averaging the strain errors in this study resulted in high standard deviations and confidence intervals, making differences in error uncertainty between the two CESA solutions difficult to determine. Increasing the sample size would be beneficial for reducing these errors. The accumulation of PTA at the osteochondral interface, as seen in other studies (Nieminen et al., 2017; das Neves Borges et al., 2014) caused brighter regions at the osteochondral interface. However, when the articular cartilage and subchondral bone regions were segmented and masked separately, based on the different mechanical responses of the tissues, the regions of highest error uncertainty were observed in the articular cartilage, in which the inter-specimen variation (for both MAER and SDER) was higher in Hf-WD POM-stained specimens, particular at lower subvolumes (~50–100 voxels). Therefore, consistent staining of the cartilage matrix should be a primary focus when comparing different CESA solutions for DVC.

The use of a PTA/ethanol staining solution modified the mechanical properties of the tissue at both the micro- and nano-scale, increasing

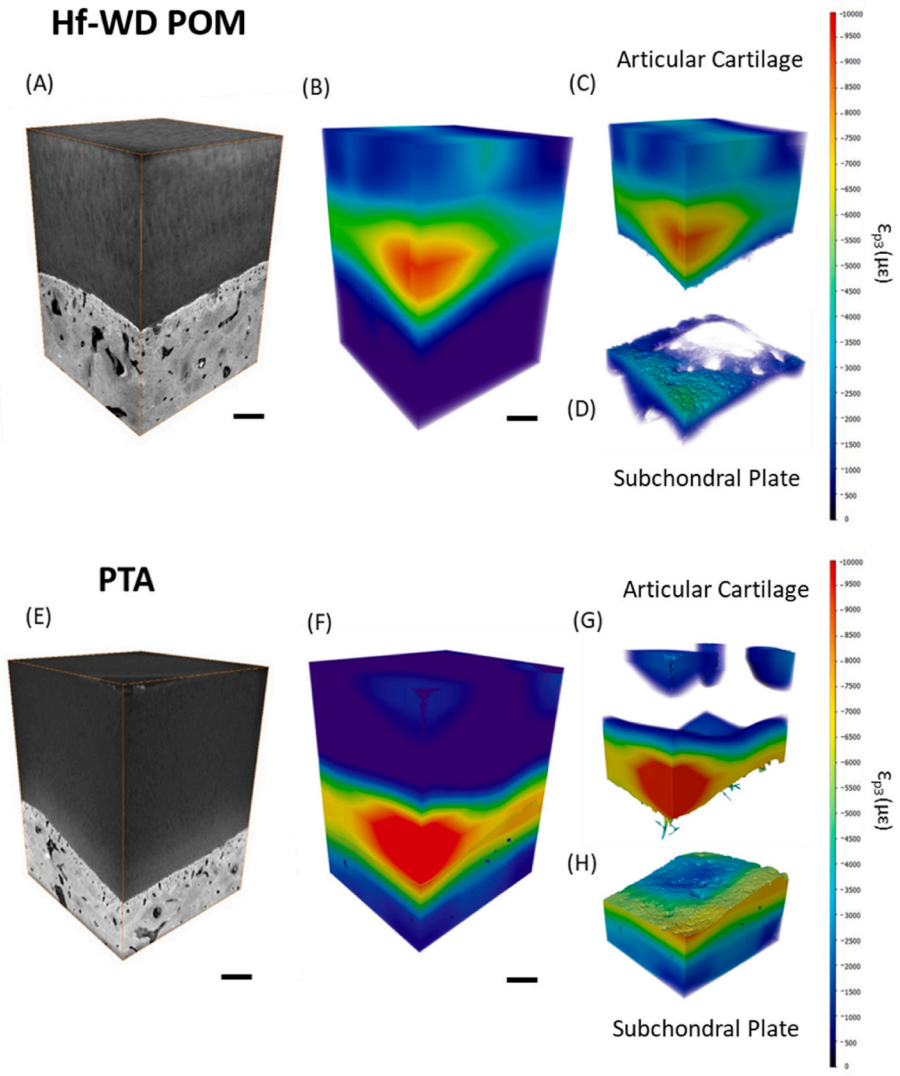

Fig. 6. 3D full-field residual strain distribution of the Third Principal Strain (ε_{p3}) after unconfined compression on a representative sample. Reconstructed CECT greyscale images showing volume of the osteochondral specimen (A) and strain distribution patterns of ε_{p3} in the entire volume (B) and in the cartilage (C) and mineralised regions of calcified cartilage and subchondral bone (D) computed using a multi-pass scheme with 90 voxel final sub-volume size (Scale bars = 300 μm).

stiffness, hardness, and the reduced indentation modulus of articular cartilage (Figs. 3 and 4). This disproportionate change in tissue stiffness of the articular cartilage in comparison to the subchondral bone is an important factor for affecting the strain distribution throughout the entire osteochondral unit, which using a PTA/ethanol staining solution, showed more concentrated residual strains (up to ~10,000 με) of ε_{p3} located in the deep zones at the cartilage-bone interface and shear strain distributed throughout a larger volume of the articular cartilage. This is relevant since there are few studies on the strain distribution at the cartilage-bone interface using DVC. However, these results are consistent with compressive strain values reported in the literature, with residual strains of up to ~7000 με detected in localised regions in articular cartilage when loaded at 1% strain (Tozzi et al., 2020) and up to ~9000 με observed in areas of calcified cartilage, decreasing throughout the subchondral bone (Madi et al., 2020). The purpose of investigating this stain distribution across the osteochondral interface is to be able to detect and compare strain changes in early-OA, however, this can only be done accurately when a suitable contrasting enhancing stain is used that doesn't affect the mechanical properties of cartilage and bone. Therefore, this proof-of-concept study is important for validating staining methods to be able to apply these techniques to OA specimens in future studies.

The interaction between PTA and organic cations in articular cartilage is pH dependent (Quintarelli et al., 2016) and, it is known that PTA binds to collagen via a two-step mechanism, firstly by intersubfibrillar binding of polyanions to basic groups, then by intra-subfibrillar binding to relaxed fibres (Nemetschek et al., 1979). However, the increased stiffness of articular cartilage and alteration in biomechanical properties as shown in this study may also be due to ethanol which is commonly used as the solvent for PTA staining procedures (Clark et al., 2021). Ethanol dehydrates and can deform matrix components of the articular cartilage (Nieminen et al., 2017). High concentrations (≥60 %, v/v) of ethanol cause accelerated self-association of the collagen triple helices, and result in increased and denser fibril formation due to dehydration-induced hydrophobic association of collagen molecules (Gopinath et al., 2014). In contrast, staining with a Hf-WD POM/PBS solution did not have a significant influence of the mechanical properties (stiffness, hardness, and indentation modulus) of the bone and the cartilage (Fig. 4), indicating this may be a preferred CESA solution for increasing contrast for CECT imaging, whilst maintaining the native mechanical properties of the tissue.

There were limitations to this study. Firstly, only a small number of bovine osteochondral specimens were used for both nanoindentation (n = 3) and for CECT imaging/DVC (n = 6). Therefore, further studies with

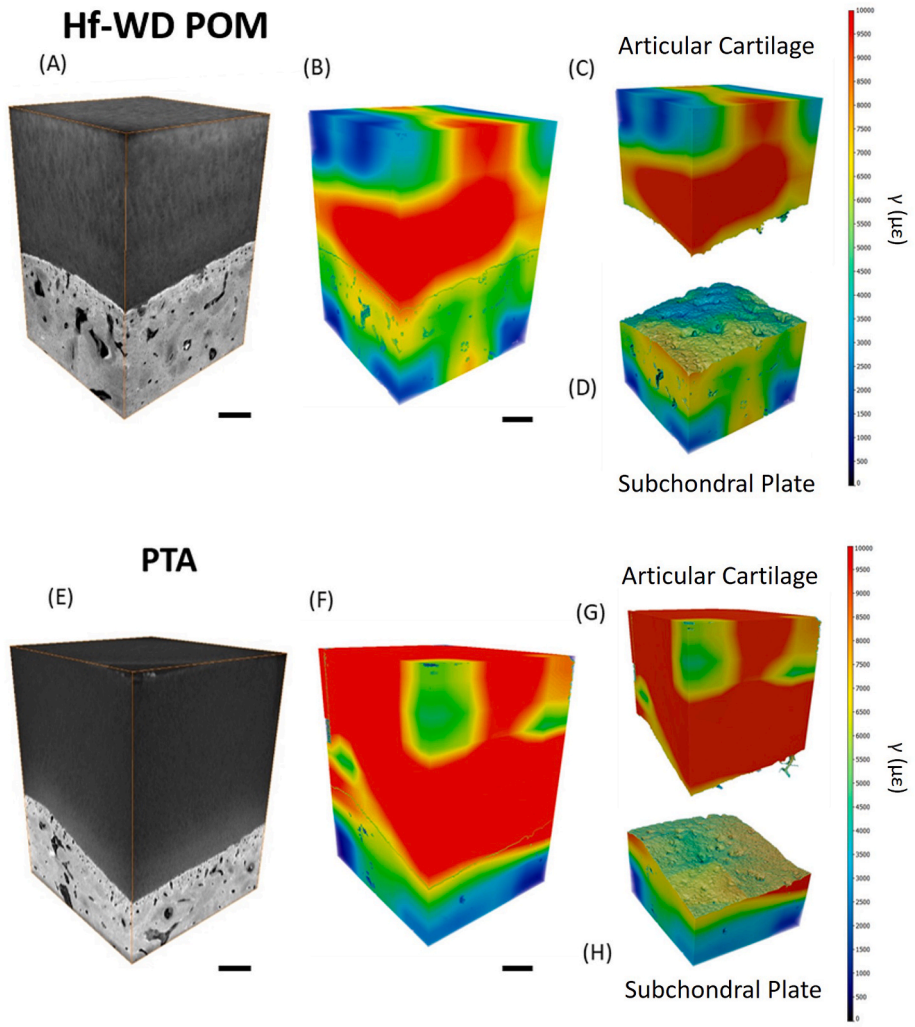

Fig. 7. Strain distribution of shear strain (γ) in a representative sample of Hf-WD POM- (A–D) and PTA-stained (E–H) osteochondral plugs. Reconstructed CECT images (A, E) with corresponding shear strain distribution in entire volume (B) and individual volumes for cartilage (C) and mineralised regions of calcified cartilage and subchondral bone (D). (Computed using multi-pass scheme with 90-voxel final sub-volume size; Scale bars = 300 μm).

increased specimen numbers may be needed to support these results. Additionally, the nanoindentation method involved using hydrated specimens which were moist, and tested in air. A Berkovich tip was used for consistency between tissue types, which although suitable for the subchondral bone measurements, and mineralised tissues (Ferguson et al., 2003; Gupta et al., 2005; Campbell et al., 2012), and has been used in other studies for the nanoindentation of cartilage (Mieloch et al.; Franke et al., 2011; Franke et al., 2007; Han et al., 2011a), is not ideal for soft or viscoelastic tissues, as it can over-estimate the contact area (Gupta et al., 2005; Franke et al., 2011; Han et al., 2011b). However, this effect is minimal since our study was comparative and only relative values were expressed, nonetheless, using a spherical fluid probe would be beneficial for future research for reporting absolute values. It is also important to note that differences in sample preparation (including surface roughness) (Darling et al., 2010; Chandran et al., 2018), indentation conditions (embedded, dry or liquid) (Campbell et al., 2012; Hengsberger et al., 2002), tip geometry and size (Simha et al., 2007; Bae et al., 2006), direction (transverse or axial) and indentation depth (Chandran et al., 2018) between studies can have a critical effect on the absolute value obtained. Despite these constraints, the nanoindentation technique used in this study still provides relative comparison for pre- and post-stain mechanical properties. These results are consistent with the post-stain alterations in cartilage stiffness on the microscale, and have similar fresh cartilage stiffness values to that reported in the literature from micro-indentation tests (~0.7–1.3 MPa) (Yuh et al., 2021; Loparic et al., 2010; Miller and Morgan, 2010).

The inter-specimen variability in thickness and biochemical composition may also affect the penetration time of CESAs throughout the tissue making it difficult to accurately reproduce CECT images with consistent staining (Nieminen et al., 2015). Although XCT is labelled as a non-destructive form of imaging, other studies have shown that X-ray radiation can cause alterations in mechanical properties of articular cartilage and subchondral bone (Lindburg et al., 2013; Cicek, 2016; Cash and Dean, 2019), including low voltages similar to those used in this study. Prolonged or excessive X-ray exposure can also cause heating, resulting in artificial displacement and strain measurements for DVC (Wang et al., 2018), predominantly in the superficial zone (Clark et al., 2021), which was addressed and eliminated in this study by performing zero-strain tests. In this study, the scan time was limited to <4 h per specimen, which was the minimum time to achieve sufficient resolution of articular cartilage features within a suitable field of view. This is important also because postmortem changes in the tissue are likely to be reduced with decreased exposure time. Additionally, since cartilage is a viscoelastic material, the long exposure times necessary to obtain sufficient image contrast are often associated with stress relaxation.

Overall, these findings provide a comparison between a Hf-WD POM/PBS and more conventionally used PTA/ethanol staining solution to show the potential for CECT to be able to resolve microstructural

features in articular cartilage, making DVC computation and strain analysis at the osteochondral interface possible. This study highlights the importance of mechanical assessment of articular cartilage and subchondral plate/bone post-staining as changes to tissue mechanical properties may alter load transfer and disrupt strain distribution throughout the osteochondral unit. In this instance, the use of 1:2 Hf-WD POM was more mechanically suitable for enhancing contrast for CECT imaging and subsequent DVC strain analysis.

This study is useful for further improving CESA solutions, to provide reliable methodologies for CECT imaging and DVC to gain a deeper understanding of pathological interactions and strain distribution at the cartilage-bone interface.

Funding

This research was funded by the University of Portsmouth and received no external funding. TB acknowledges the French Community of Belgium in the framework of a FRIA grant (40004158). TB and GK acknowledge the support from a Research Foundation Flanders (FWO) project (grant G088218N).

CRediT authorship contribution statement

Sarah Davis: Writing – review & editing, Writing – original draft, Methodology, Investigation, Formal analysis, Data curation, Conceptualization. **Aikaterina Karali:** Writing – review & editing, Supervision. **Tim Balcaen:** Writing – review & editing, Resources. **Jurgita Zekonyte:** Writing – review & editing, Software, Resources, Methodology, Data curation. **Maïté Pétré:** Writing – review & editing. **Marta Roldo:** Writing – review & editing, Supervision, Resources, Funding acquisition. **Greet Kerckhofs:** Writing – review & editing, Resources, Conceptualization. **Gordon Blunn:** Writing – review & editing, Visualization, Validation, Supervision, Resources, Methodology, Funding acquisition, Conceptualization.

Declaration of competing interest

The authors declare that they have no known competing financial interests or personal relationships that could have appeared to influence the work reported in this paper.

Data availability

Data will be made available on request.

Acknowledgements

Thanks to Prof. Wim De Borggraeve (KU Leuven, Belgium) for his expertise in the synthesis of the Hf-WD POM, Colin Lupton for technical assistance during mechanical testing.

References

Bae, W.C., Lewis, C.W., Levenston, M.E., Sah, R.L., 2006. Indentation testing of human articular cartilage: effects of probe tip geometry and indentation depth on intra-tissue strain. J. Biomech. 39 (6), 1039–1047. Available from: https://pubmed.ncbi.nlm.nih.gov/16549094/.

Burgin, L.v., Aspden, R.M., 2007. A drop tower for controlled impact testing of biological tissues. Med. Eng. Phys. 29 (4), 525–530. Available from: https://pubmed.ncbi.nlm.nih.gov/16876457/.

Burr, D.B., Gallant, M.A., 2012. Bone remodelling in osteoarthritis. Nat. Rev. Rheumatol. 8 (11), 665–673. Available from: https://www.nature.com/articles/nrrheum.2012.130.

Campbell, S.E., Ferguson, V.L., Hurley, D.C., 2012. Nanomechanical mapping of the osteochondral interface with contact resonance force microscopy and nanoindentation. Acta Biomater. 8 (12), 4389–4396.

Cash, H., Dean, D., 2019. The effects of low-dose radiation on articular cartilage: a review. J. Biol. Eng. 13 (1), 1–8. Available from: https://jbioleng.biomedcentral.com/articles/10.1186/s13036-018-0125-4.

Chandran, P.L., Dimitriadis, E.K., Mertz, E.L., Horkay, F., 2018. Microscale mapping of extracellular matrix elasticity of mouse joint cartilage: an approach to extracting bulk elasticity of soft matter with surface roughness [Internet] Soft Matter [cited 2023 Mar 7];14(15):2879–92. Available from: https://pubs.rsc.org/en/content/articlehtml/2018/sm/c7sm02045g.

Cicek, E., 2016. Effect of X-ray irradiation on articular cartilage mechanical properties. Acta Phys. Pol., A 129 (2), 200–202.

Clark, J.N., Garbout, A., Ferreira, S.A., Javaheri, B., Pitsillides, A.A., Rankin, S.M., et al., 2020. Propagation phase-contrast micro-computed tomography allows laboratory-based three-dimensional imaging of articular cartilage down to the cellular level. Osteoarthritis Cartilage 28 (1), 102–111.

Clark, J.N., Tavana, S., Clark, B., Briggs, T., Jeffers, J.R.T., Hansen, U., 2021. High resolution three-dimensional strain measurements in human articular cartilage. J. Mech. Behav. Biomed. Mater. 124, 104806. Available from: https://pubmed.ncbi.nlm.nih.gov/34509906/.

Dall'Ara, E., Barber, D., Viceconti, M., 2014. About the inevitable compromise between spatial resolution and accuracy of strain measurement for bone tissue: a 3D zero-strain study. J. Biomech. 47 (12), 2956–2963.

Dall'Ara, E., Peña-Fernández, M., Palanca, M., Giorgi, M., Cristofolini, L., Tozzi, G., 2017. Precision of digital volume correlation approaches for strain analysis in bone imaged with micro-computed tomography at different dimensional levels. Front Mater 4, 31.

Darling, E.M., Wilusz, R.E., Bolognesi, M.P., Zauscher, S., Guilak, F., 2010. Spatial mapping of the biomechanical properties of the pericellular matrix of articular cartilage measured in situ via atomic force microscopy. Biophys. J. 98 (12), 2848–2856. Available from: https://pubmed.ncbi.nlm.nih.gov/20550897/.

das Neves Borges, P., Forte, A.E., Vincent, T.L., Dini, D., Marenzana, M., 2014. Rapid, automated imaging of mouse articular cartilage by microCT for early detection of osteoarthritis and finite element modelling of joint mechanics. Osteoarthritis Cartilage 22 (10), 1419–1428.

Davis, S., Roldo, M., Blunn, G., Tozzi, G., Roncada, T., 2021. Influence of the mechanical environment on the regeneration of osteochondral defects. Front. Bioeng. Biotechnol. 9, 10.

de Bournonville, S., Vangrunderbeeck, S., Ly, H.G.T., Geeroms, C., de Borggraeve, W.M., Parac-Vogt, T.N., et al., 2020. Exploring polyoxometalates as non-destructive staining agents for contrast-enhanced microfocus computed tomography of biological tissues. Acta Biomater. 105, 253–262.

Ferguson, V.L., Bushby, A.J., Boyde, A., 2003. Nanomechanical properties and mineral concentration in articular calcified cartilage and subchondral bone. J. Anat. 203 (2), 191. Available from: /pmc/articles/PMC1571155/.

Franke, O., Durst, K., Maier, V., Göken, M., Birkholz, T., Schneider, H., et al., 2007. Mechanical properties of hyaline and repair cartilage studied by nanoindentation. Acta Biomater. 3 (6), 873–881.

Franke, O., Göken, M., Meyers, M.A., Durst, K., Hodge, A.M., 2011. Dynamic nanoindentation of articular porcine cartilage. Mater. Sci. Eng. C 31 (4), 789–795.

Gao, L.L., Zhang, C.Q., Yang, Y.B., Shi, J.P., Jia, Y.W., 2013. Depth-dependent strain fields of articular cartilage under rolling load by the optimized digital image correlation technique. Mater. Sci. Eng. C 33 (4), 2317–2322.

Gao, X., Patwa, A.N., Deng, Z., Utsunomiya, H., Grinstaff, M.W., Ruzbarsky, J.J., et al., 2021. Influence of fixation on CA4+ contrast enhanced microCT of articular cartilage and subsequent feasibility for histological evaluation. Am. J. Transl. Res. 13 (8), 8921. Available from: /pmc/articles/PMC8430171/.

Gillard, F., Boardman, R., Mavrogordato, M., Hollis, D., Sinclair, I., Pierron, F., et al., 2014. The application of digital volume correlation (DVC) to study the microstructural behaviour of trabecular bone during compression. J. Mech. Behav. Biomed. Mater. 29, 480–499.

Goldring, S.R., Goldring, M.B., 2016. Changes in the osteochondral unit during osteoarthritis: structure, function and cartilage–bone crosstalk. Nat. Rev. Rheumatol. 12 (11), 632–644. Available from: https://www.nature.com/articles/nrrheum.2016.148.

Gopinath, A., Reddy, S.M.M., Madhan, B., Shanmguam, G., Rao, J.R., 2014. Effect of aqueous ethanol on the triple helical structure of collagen. Eur. Biophys. J. 43 (12), 643–652. Available from: https://link.springer.com/article/10.1007/s00249-014-0994-5.

Gupta, H.S., Schratter, S., Tesch, W., Roschger, P., Berzlanovich, A., Schoeberl, T., et al., 2005. Two different correlations between nanoindentation modulus and mineral content in the bone–cartilage interface. J. Struct. Biol. 149 (2), 138–148.

Han, L., Frank, E.H., Greene, J.J., Lee, H.Y., Hung, H.H., Grodzinsky, A.J., Ortiz, C., 2011a. Time-dependent nanomechanics of cartilage. Biophys. J. 100 (7), 1846–1854. https://doi.org/10.1016/j.bpj.2011.02.031.

Han, E., Chen, S.S., Klisch, S.M., Sah, R.L., 2011b. Contribution of proteoglycan osmotic swelling pressure to the compressive properties of articular cartilage. Biophys. J. 101 (4), 916–924.

Hengsberger, S., Kulik, A., Zysset, P h, 2002. Nanoindentation discriminates the elastic properties of individual human bone lamellae under dry and physiological conditions. Bone 30 (1), 178–184.

Hunter, D.J., Schofield, D., Callander, E., 2014. The individual and socioeconomic impact of osteoarthritis. Nat. Rev. Rheumatol. 10 (7), 437–441. Available from: https://www.nature.com/articles/nrrheum.2014.44.

Hunter, D.J., March, L., Chew, M., 2020. Osteoarthritis in 2020 and beyond: a Lancet Commission. Lancet 396 (10264), 1711–1712.

Kato, C.N., Shinohara, A., Hayashi, K., Nomiya, K., 2006. Syntheses and X-ray crystal structures of zirconium(IV) and hafnium(IV) complexes containing monovacant wells-Dawson and Keggin polyoxotungstates. Inorg. Chem. 45 (20), 8108–8119. Available from: https://europepmc.org/article/MED/16999408.

Kerckhofs, G., Stegen, S., van Gastel, N., Sap, A., Falgayrac, G., Penel, G., et al., 2018. Simultaneous three-dimensional visualization of mineralized and soft skeletal tissues by a novel microCT contrast agent with polyoxometalate structure. Biomaterials 159, 1–12.

Lindburg, C.A., Willey, J.S., Dean, D., 2013. Effects of low dose X-ray irradiation on porcine articular cartilage explants. J. Orthop. Res. 31 (11), 1780–1785. Available from: https://onlinelibrary.wiley.com/doi/full/10.1002/jor.22406.

Liu, L., Morgan, E.F., 2007. Accuracy and precision of digital volume correlation in quantifying displacements and strains in trabecular bone. J. Biomech. 40 (15), 3516–3520.

Loparic, M., Wirz, D., Daniels, A.U., Raiteri, R., Vanlandingham, M.R., Guex, G., et al., 2010. Micro- and Nanomechanical analysis of articular cartilage by indentation-type atomic force microscopy: validation with a gel-microfiber composite. Biophys. J. 98 (11), 2731. Available from: /pmc/articles/PMC2877335/.

Lusic, H., Grinstaff, M.W., 2013. X-ray-computed tomography contrast agents. Chem. Rev. 113 (3), 1641–1666. Available from: https://pubs.acs.org/doi/full/10.1021/cr200358s.

Madi, K., Staines, K.A., Bay, B.K., Javaheri, B., Geng, H., Bodey, A.J., Cartmell, S., Pitsillides, A.A., Lee, P.D., 2020. In situ characterization of nanoscale strains in loaded whole joints via synchrotron X-ray tomography. Nat. Biomed. Eng. 4 (3), 343–354. https://doi.org/10.1038/s41551-019-0477-1.

Martel-Pelletier, J., Barr, A.J., Cicuttini, F.M., Conaghan, P.G., Cooper, C., Goldring, M. B., et al., 2016. Osteoarthritis. Nat. Rev. Dis. Prim. 2 (1), 1–18. Available from: https://www.nature.com/articles/nrdp201672.

Miller, G.J., Morgan, E.F., 2010. Use of microindentation to characterize the mechanical properties of articular cartilage: comparison of biphasic material properties across length scales. Osteoarthritis Cartilage 18 (8), 1051–1057.

Nemetschek, T., Riedl, H., Jonak, R., 1979. Topochemistry of the binding of phosphotungstic acid to collagen. J. Mol. Biol. 133 (1), 67–83.

Nieminen, H.J., Ylitalo, T., Suuronen, J.P., Rahunen, K., Salmi, A., Saarakkala, S., et al., 2015. Delivering agents locally into articular cartilage by intense MHz ultrasound. Ultrasound Med. Biol. 41 (8), 2259–2265.

Nieminen, H.J., Gahunia, H.K., Pritzker, K.P.H., Ylitalo, T., Rieppo, L., Karhula, S.S., et al., 2017. 3D histopathological grading of osteochondral tissue using contrast-enhanced micro-computed tomography. Osteoarthritis Cartilage 25 (10), 1680–1689.

Oliver, W.C., Pharr, G.M., 2004. Measurement of hardness and elastic modulus by instrumented indentation: advances in understanding and refinements to methodology. J. Mater. Res. 19 (1), 3–20.

Pauwels, E., van Loo, D., Cornillie, P., Brabant, L., van Hoorebeke, L., 2013. An exploratory study of contrast agents for soft tissue visualization by means of high resolution X-ray computed tomography imaging. J. Microsc. 250 (1), 21–31. Available from: https://onlinelibrary.wiley.com/doi/full/10.1111/jmi.12013.

Peña Fernández, M., Dall'Ara, E., Bodey, A.J., Parwani, R., Barber, A.H., Blunn, G.W., et al., 2019. Full-field strain analysis of bone-biomaterial systems produced by the implantation of osteoregenerative biomaterials in an ovine model. ACS Biomater. Sci. Eng. 5 (5), 2543–2554. Available from: https://pubs.acs.org/doi/full/10.1021/acsbiomaterials.8b01044.

Peña Fernández, M., Kao, A.P., Witte, F., Arora, H., Tozzi, G., 2020. Low-cycle full-field residual strains in cortical bone and their influence on tissue fracture evaluated via in situ stepwise and continuous X-ray computed tomography. J. Biomech. 113, 110105.

Quintarelli, G., Zito, R., Cifonelli, J.A., 2016. On phosphotungstic acid staining. I. J. Histochem. Cytochem. 19 (11), 641–647. Available from: https://journals.sagepub.com/doi/10.1177/19.11.641.

Santos, S., Emery, N., Neu, C.P., Pierce, D.M., 2019. Propagation of microcracks in collagen networks of cartilage under mechanical loads. Osteoarthritis Cartilage 27 (9), 1392–1402.

Schindelin, J., Arganda-Carreras, I., Frise, E., Kaynig, V., Longair, M., Pietzsch, T., et al., 2012. Fiji: an open-source platform for biological-image analysis. Nat. Methods 9 (7), 676–682. Available from: https://www.nature.com/articles/nmeth.2019.

Schmitz, N., Laverty, S., Kraus, V.B., Aigner, T., 2010. Basic methods in histopathology of joint tissues. Osteoarthritis Cartilage 18 (Suppl. 3), S113–S116.

Shaktivesh, Malekipour F., Lee, P.V.S., 2019. Shock absorbing ability in healthy and damaged cartilage-bone under high-rate compression. J. Mech. Behav. Biomed. Mater. 90, 388–394.

Simha, N.K., Jin, H., Hall, M.L., Chiravarambath, S., Lewis, J.L., 2007. Effect of indenter size on elastic modulus of cartilage measured by indentation. J. Biomech. Eng. 129 (5), 767–775. Available from: https://asmedigitalcollection.asme.org/biomechanical/article/129/5/767/469821/Effect-of-Indenter-Size-on-Elastic-Modulus-of.

Stewart, R.C., Patwa, A.N., Lusic, H., Freedman, J.D., Wathier, M., Snyder, B.D., et al., 2017. Synthesis and preclinical characterization of a cationic iodinated imaging contrast agent (CA4+) and its use for quantitative computed tomography of ex vivo human hip cartilage. J. Med. Chem. 60 (13), 5543–5555. Available from: https://pubs.acs.org/doi/full/10.1021/acs.jmedchem.7b00234.

Sztefek, P., Vanleene, M., Olsson, R., Collinson, R., Pitsillides, A.A., Shefelbine, S., 2010. Using digital image correlation to determine bone surface strains during loading and after adaptation of the mouse tibia. J. Biomech. 43 (4), 599–605.

Tavana, S., Clark, J.N., Newell, N., Calder, J.D., Hansen, U., 2020. In Vivo deformation and strain measurements in human bone using digital volume correlation (DVC) and 3T clinical MRI. Materials 13 (23), 5354. Available from: https://www.mdpi.com/1996-1944/13/23/5354/htm.

Tozzi, G., Peña Fernández, M., Davis, S., Karali, A., Kao, A.P., Blunn, G., 2020. Full-field strain uncertainties and residuals at the cartilage-bone interface in unstained tissues using propagation-based phase-contrast XCT and digital volume correlation. Materials 13 (11), 2579. https://doi.org/10.3390/ma13112579.

Varga, F., Držík, M., Handl, M., Chlpík, J., Kos, P., Filová, E., et al., 2007. Biomechanical characterization of cartilages by a novel approach of blunt impact testing. Physiol. Res. 56 (Suppl 1(SUPPL. 1)). Available from: https://pubmed.ncbi.nlm.nih.gov/17552893/.

Wang, Y., Wluka, A.E., Pelletier, J.P., Martel-Pelletier, J., Abram, F., Ding, C., et al., 2010. Meniscal extrusion predicts increases in subchondral bone marrow lesions and bone cysts and expansion of subchondral bone in osteoarthritic knees. Rheumatology 49 (5), 997–1004. Available from: https://academic.oup.com/rheumatology/article/49/5/997/1787505.

Wang, B., Pan, B., Lubineau, G., 2018. In-situ systematic error correction for digital volume correlation using a reference sample. Exp. Mech. 58 (3), 427–436. Available from: https://link.springer.com/article/10.1007/s11340-017-0356-1.

Yoo, HJ, Hong, SH, Choi, JY, Lee, IJ, Kim, SJ, Choi, JA, et al., 2011. Contrast-enhanced CT of articular cartilage: experimental study for quantification of glycosaminoglycan content in articular cartilage. Radiology 261 (3), 805–812. Available from: https://pubs.rsna.org/doi/10.1148/radiol.11102495.

Yuh, C., O'Bryan, C.S., Angelini, T.E., Wimmer, M.A., 2021. Microindentation of cartilage before and after articular loading in a bioreactor: assessment of length-scale dependency using two analysis methods. Exp. Mech. 61 (7), 1069–1080. Available from: https://pubmed.ncbi.nlm.nih.gov/35528779/.

Zhen, G., Guo, Q., Li, Y., Wu, C., Zhu, S., Wang, R., et al., 2021. Mechanical stress determines the configuration of TGFβ activation in articular cartilage. Nat. Commun. 12 (1), 1–16. Available from: https://www.nature.com/articles/s41467-021-21948-0.